

## RADIATIVE TRANSFER IN PROTOPLANETARY DISKS

C. Pinte<sup>1</sup>, F. Ménard<sup>1</sup> and G. Duchêne<sup>1</sup>

**Abstract.** We present a new 3D continuum radiative transfer code, MCFOST, based on a Monte-Carlo method. The reliability and efficiency of the code is tested by comparison with five different radiative transfer codes previously tested by Pascucci et al. (2004), using a 2D disk configuration. When tested against the same disk configuration, no significant difference is found between the temperature and SED calculated with MCFOST and with the other codes. The computed values are well within the range of values computed by the other codes. The code-to-code differences are small, they rarely exceed 10% and are usually much smaller.

### 1 Introduction

Dust is present everywhere in astrophysics, from the interstellar medium to the atmospheres and close circumstellar environments of numerous classes of objects; from the lower mass planets and brown dwarfs, to massive stars. With the advent of high angular resolution and high contrast imagers, the basic structural properties (e.g., size, inclination, and surface brightness) of the circumstellar environments of the nearest and/or largest objects — disks and envelopes around young stars in nearby star forming regions and around more distant evolved stars — are now under close scrutiny. With this unprecedented wealth of high resolution data, from optical to radio, fine studies of the dust content become possible and potent radiative transfer (RT) codes are needed to fully exploit the data.

At short wavelengths, dust grains efficiently absorb, scatter, and polarise the starlight while at longer wavelengths dust re-emits the absorbed radiation. How much radiation is scattered and absorbed is a function of both the geometry of the circumstellar environment and the properties of the dust. In turns, the amount of absorbed radiation sets the temperature of the dust (and gas) and defines the amount of radiation that is re-emitted at longer, thermal, wavelengths.

---

<sup>1</sup> Laboratoire d'Astrophysique de Grenoble, CNRS/UJF UMR 5571, 414 rue de la Piscine, B.P. 53, F-38041 Grenoble Cedex 9, France

To get a reliable understanding of the structure and evolution of these “dusty” objects, be it the evolution of dust sizes, the temperature dependent chemistry, or simply the density profiles, it is highly desirable to model not only the integrated fluxes (*i.e.*, the spectral energy distributions), but also the resolved brightness maps and polarisation profiles when available. This can only be done by solving the radiative transfer (hereafter RT) problem in media that can have large optical depths and/or complex geometries and compositions. Needless to say, analytical solutions do not always exist and sophisticated numerical methods must generally be used. One such versatile numerical method is the Monte Carlo method. The code we describe and test below is based on that RT scheme.

The original version of the code, MCFOST, treated the polarised continuum RT problem by including scattering only, without a calculation of the temperature structure and thermal emission from the circumstellar environment Ménard (1989). That code was used extensively to produce synthetic images of the scattered light from disks around young stars. Examples include the circumbinary ring of GG Tau Duchêne et al. (2004), the large silhouette disk associated with IRAS 04158+2805 (Ménard et al. 2005), and an analysis of the circular polarisation in GSS 30 Chrysostomou et al. (1997). In this paper we present a new improved version of MCFOST that includes passive heating of the circumstellar environment by stellar radiation and thermal re-emission from the dust, needed to prepare future observations with Spitzer, Hershel and Alma.

To validate MCFOST, we perform a comparison with five other RT codes, including three using a Monte Carlo method that were benchmarked in a previous study Pascucci et al. (2004) (hereafter P04). To compare the reliability and efficiency of each code, P04 used a well defined 2-dimensional disk configuration, with simple dust properties. Each code calculated the temperature structure in the disk, as well as the emergent SED. The results were compared quantitatively as a function of optical thickness and disk inclination. The agreement is generally better than 10% for the most difficult cases, *i.e.*, large optical depths, and much better in the optically thin cases. We performed identical calculations with MCFOST and present the results and comparisons below.

In §2, we briefly describe MCFOST. In section §3, we recall the benchmark problem used to compare MCFOST with the 5 RT codes included in P04. Results are presented in §4, they include the temperature profile and SED for a range of disk optical thicknesses.

## 2 Description of the numerical code

MCFOST is a 3D continuum radiative transfer numerical code based on the Monte-Carlo method. It was originally developed by Ménard (1989) to model the scattered light in dusty media (including linear and circular polarisations). In this paper, we present an extended version of the code that includes dust heating and continuum thermal re-emission.

### 2.1 Geometry of the computation grid

The spatial grid is defined in cylindrical coordinates. It is well adapted to the geometry of circumstellar disks. We use  $N_r$  logarithmically spaced radial grid cells and  $N_z$  linearly spaced vertical grid cells. The size of the vertical cells follow the flaring of the disk, with a cutoff at 10 times the local scale height. For the purpose of the benchmark calculations presented in this paper, axisymmetry is assumed. However, MCFOST allows the density distribution to be defined arbitrarily in 3D, with the limitation that within each cell, quantities are held constant. For example, MCFOST in a 3D version has already been used to study the photometric behaviour of AA Tau Pinte & Ménard (2004).

### 2.2 Position dependence of the dust distribution

An explicit spatial dependence of the size distribution  $f(a, \vec{r})$  is implemented in MCFOST. The dust properties are therefore defined locally, *i.e.*, each cell of the disk may contain its own independent dust population. This allows to model dust settling towards the midplane of the disk and/or variations of the chemical composition of the dust from the inner, hot regions to the outer, cold edge of the disk.

### 2.3 Optical dust properties

Dust particles can be arbitrary shaped and are assumed to be randomly oriented. In the case of homogeneous and spherical particles, the dust optical properties are computed with Mie theory. The optical properties in any cell of the disk are derived in accordance with the local size and composition distributions  $f(a, \vec{r})$ , at the expense of a significant usage of memory space. The extinction and scattering opacities are given by

$$\kappa^{\text{ext/sca}}(\lambda, \vec{r}) = \int_{a_{\min}}^{a_{\max}} \pi a^2 Q_{\text{ext/sca}}(\lambda, a) f(a, \vec{r}) da \quad (2.1)$$

and the local Muller matrix is

$$S(\lambda, \vec{r}) = \int_{a_{\min}}^{a_{\max}} S(\lambda, a) f(a, \vec{r}) da \quad (2.2)$$

where  $Q_{\text{sca}}(\lambda, a)$ ,  $Q_{\text{ext}}(\lambda, a)$  and  $S(\lambda, a)$  are respectively the scattering and extinction cross sections and the Mueller matrix of a grain of size  $a$  at a wavelength  $\lambda$ .

### 2.4 The radiative transfer scheme in MCFOST

The Monte Carlo method allows to follow individual monochromatic “photon packets” that propagate through the circumstellar environment until they exit the computation grid. The propagation process is governed by scattering, absorption

and re-emission events that are controlled by the optical properties of the medium (opacity, albedo, scattering phase function, etc...) and by the temperature distribution. Upon leaving the circumstellar environment, photon packets are recorded into frequency dependent synthetic images and SED's can be constructed.

To improve its computational efficiency, MCFOST uses different strategies to set the energy of a photon packet, corresponding to different samplings of the radiation field. The energy of a packet, hence the number of photons it contains, is chosen and optimised depending on the goal of the calculations. On the one hand, the convergence of the temperature distribution is optimized when all photon packets have the same *energy*, independently of their wavelengths. This procedure insures that more photon packets are emitted in the more luminous bins. On the other hand, the computation of SEDs is more efficient when it is the *number* of photon packets that is held constant for all wavelength bins. In that case it is the energy of the packets that is wavelength dependent. Thus, MCFOST is more efficient when it computes the temperature and SED with a two-step process:

- **Step 1** is the temperature determination. Photon packets are generated and calculated one by one. They are generated at the stellar photosphere and followed until they exit the computation grid. Upon scattering in the disk, the propagation vector of the packet is modified, but not its wavelength. Upon absorption however, packets are immediately re-emitted, in situ and isotropically, but at a different wavelength, calculated according to the temperature of the grid cell. For this re-emission process, the concept of *immediate reemission* and the associated *temperature correction method* proposed by Bjorkman & Wood (2001) are used. They are presented as *scheme 3* in P04. In this step, all photon packets have a similar energy and are randomly scattered/absorbed within the disk. The concept of *mean intensity* suggested by Lucy (1999) is further used to reduce noise in the temperature estimation for optically thin cases. Step 1 allows for a fast convergence of the temperature but is rather time-consuming when used to derive SEDs, especially in the low-energy, long wavelength regime. Therefore SEDs are calculated differently.
- **Step 2** computes the SED and/or images from the temperature distribution calculated in step 1. In step 2, the number of photon packets is held constant at all wavelengths and the *enforced scattering* concept of Cashwell & Everett (1959) is implemented to further speed up convergence. Step 2 maintains a similar noise level per wavelength bin and reduces convergence time for the SED by limiting the CPU time spent in high luminosity bins and focussing on low luminosity bins.

#### 2.4.1 The emission of photon packets

In MCFOST, two radiation sources are considered, the star and the circumstellar environment. The stellar photosphere can be represented by (i) a sphere radiating uniformly or (ii) a limb-darkened sphere or (iii) a point-like source, whichever is

relevant for the problem under consideration. Hot and/or cold spots can be added to the photosphere. In the following, we consider a unique central point-like star that radiates like a black body.

In step 1 of the previous subsection, all photon packets are emitted isotropically by the central star and have the same energy, independently of their wavelength. We define the luminosity of a packet,  $\epsilon$ , as:

$$\epsilon = L_*/N_{\gamma step1} \quad (2.3)$$

where  $L_*$  is the bolometric luminosity of the star and  $N_{\gamma step1}$  the number of packets generated. The wavelength of the packet is chosen according to a normalised probability density function proportional to  $B_\lambda(T_*)$ .

In step 2, the SED is constructed using a constant number  $N_{\gamma step2}$  of packets for all the wavelength bins. The packets are emitted by the star and by the disk. The energy of the  $N_{\gamma step2}$  packets emitted at a given wavelength  $\lambda$  is determined by the total energy that the star and the disk radiates at this wavelength. The corresponding packet luminosity is :

$$\epsilon_\lambda = \frac{L_*(\lambda) + \sum_i L_i(\lambda)}{N_{\gamma step2}} \quad (2.4)$$

where  $i$  is the index of the cell and  $L_*(\lambda)$  and  $L_i(\lambda)$  are the luminosities of the star and disk cell at a given wavelength. They are given by:

$$L_*(\lambda) = 4\pi^2 R_*^2 B_\lambda(T_*) , \quad (2.5)$$

$$\text{and } L_i(\lambda) = 4\pi \kappa_i^{\text{abs}}(\lambda) B_\lambda(T_i) m_i . \quad (2.6)$$

The wavelength is set in a deterministic way and packets are randomly emitted from the star and the disk, by cell  $i$ , with the respective probabilities:

$$p_* = \frac{L_*(\lambda)}{L_*(\lambda) + \sum_i L_i(\lambda)} , \quad (2.7)$$

$$\text{and } p_i = \frac{L_i(\lambda)}{L_*(\lambda) + \sum_i L_i(\lambda)} . \quad (2.8)$$

In each disk cell we assume that the density, temperature and opacities are constant. To determine the position of emission of a photon within a given disk cell, in cylindrical geometry, the following relations are used:

$$r = \sqrt{r_{\min}^2 + A(r_{\max}^2 - r_{\min}^2)} , \quad (2.9)$$

$$|z| = z_{\min} + A(z_{\max} - z_{\min}) , \quad (2.10)$$

$$\text{and } \phi = 2\pi A \quad (2.11)$$

where  $A$  denotes three different random numbers drawn from a uniform distribution in the interval  $]0,1]$  and where  $r_{\min}$ ,  $r_{\max}$ ,  $z_{\min}$ ,  $z_{\max}$  are the radial and vertical boundaries of the cell. The dust thermal emission is assumed isotropic.

### 2.4.2 Distance between interactions

It is natural within a Monte Carlo scheme to estimate the distance a photon packet “travels” between two interactions by means of optical depth (related naturally to the density) rather than by physical, linear distance. From a site of interaction, the optical depth to the next site is randomly chosen from:

$$\tau_\lambda = -\ln A \quad (2.12)$$

with  $A \in ]0, 1]$ . The distance  $l$  is computed by integrating the infinitesimal optical depth  $\kappa^{\text{ext}}(\lambda, \vec{r})\rho(\vec{r})ds$  until the following equality is verified :

$$\tau_\lambda = \int_0^l \kappa^{\text{ext}}(\lambda, \vec{r})\rho(\vec{r})ds . \quad (2.13)$$

Once the position of interaction  $\vec{r}$  is determined, the probability that the interaction is a scattering event rather than an absorption event is estimated with the local (*i.e.*, cell) albedo :

$$p_{\text{sca}} = \mathcal{A}(\lambda, \vec{r}) = \frac{\int \pi a^2 Q_{\text{sca}}(\lambda, a) f(a, \vec{r}) da}{\int \pi a^2 Q_{\text{ext}}(\lambda, a) f(a, \vec{r}) da} . \quad (2.14)$$

In step 1, the photon packets are scattered or absorbed following this probability whereas in step 2, they are always scattered, no absorption is allowed to occur explicitly. Instead, scattering is enforced at each interaction site but the Stokes vector is weighted by the probability of scattering,  $p_{\text{sca}}$ . This allows all the photons to exit the disk and to contribute to the SED, although with a reduced weight.

### 2.4.3 Scattering

MCFOST includes a complete treatment of polarisation, including linear and circular polarisations. In the Stokes formalism used, the state of a light packet is described by its Stokes vector, with  $I$  the intensity,  $Q$  and  $U$  describing the linear polarisation, and  $V$  the circular polarisation. The interaction of a photon with a dust particle is described by a  $4 \times 4$  matrix, the Mueller matrix,  $S$ . In the simplifying case where dust particles are homogeneous and spherical (Mie Theory), the matrix becomes block-diagonal, only 4 different elements are non-zero, and only three of these are independent.

$$\begin{pmatrix} I \\ Q \\ U \\ V \end{pmatrix}_{i+1} = \begin{pmatrix} S_{11} & S_{12} & 0 & 0 \\ S_{12} & S_{11} & 0 & 0 \\ 0 & 0 & S_{33} & S_{34} \\ 0 & 0 & -S_{34} & S_{33} \end{pmatrix} \begin{pmatrix} I \\ Q \\ U \\ V \end{pmatrix}_i \quad (2.15)$$

The direction of scattering is defined by two angles  $\theta$  and  $\phi$  in spherical coordinates. Each individual element  $S_{ij}$  of the matrix is a function of the two scattering angles and of the wavelength,  $S_{ij} = S_{ij}(\theta, \phi, \lambda)$

The scattering angle  $\theta$  is randomly chosen from the pretabulated scattering phase function :

$$\Phi_\lambda(\theta) \propto S_{11}(\theta) \quad (2.16)$$

where  $S_{11}$  is the first element of the Mueller matrix.

For unpolarised incoming light packet, *i.e.*,  $Q, U = 0$ , the distribution of azimuthal angle  $\phi$  is isotropic. For light packets with a non-zero linear polarisation  $P = \sqrt{Q^2 + U^2}/I$ , the azimuthal angle is defined relative to its direction of polarisation and determined by means of the following repartition function :

$$F_\theta(\phi) = \frac{1}{2\pi} \left( \phi - \frac{S_{11}(\theta) - S_{12}(\theta)}{S_{11}(\theta) + S_{12}(\theta)} P \frac{\sin(2\phi)}{2} \right) \quad (2.17)$$

where  $\theta$  was previously chosen from equation 2.16 (see Solc (1989))

The Mueller matrix used in equation 2.15, 2.17 and 2.16 can be defined in two different ways : one Mueller matrix per grain size or one mean Mueller matrix per grid cell. In the latter case, the Mueller matrix is defined by equation 2.2. In the former case, the grain size must be chosen explicitly for each event following the probability law :

$$p(a)da = \frac{\pi a^2 Q_{\text{sca}}(a) f(a, \vec{r}) da}{\int_{a_{\min}}^{a_{\max}} \pi a^2 Q_{\text{sca}}(a) f(a, \vec{r}) da} . \quad (2.18)$$

The two methods are strictly equivalent. They can be used alternatively to optimise either the memory space or the computation time required.

#### 2.4.4 Absorption and radiative equilibrium

The temperature of the dust particles is determined by assuming radiative equilibrium and that the dust opacities do not depend on temperature.

Each time a packet  $\gamma$  of a given wavelength  $\lambda$  travels through a cell, we compute  $\Delta l_\gamma$ , the length travelled by the packet in the cell and the mean intensity  $J_\lambda$  in the cell is derived following Lucy (1999) :

$$J_\lambda = \frac{1}{4\pi V_i} \sum_\gamma \epsilon \Delta l_\gamma = \frac{1}{4\pi V_i} \sum_\gamma \frac{L_*}{N_\gamma} \Delta l_\gamma \quad (2.19)$$

where  $V_i$  is the volume of the cell  $i$ .

The dust thermal balance should take into account the thermal coupling between gas and dust. In high density regions, close to the disk midplane, the coupling is very strong and the gas temperature should be close to the dust temperature. In the surface layers of the disk, on the other hand, density becomes very low and gas-dust thermal exchanges should be reduced.

The two extreme assumptions are implemented in MCFOST : either the gas-dust thermal exchange is perfectly efficient and gas and dust are in local thermodynamic equilibrium (LTE), either there is no thermal coupling between gas and dust.

If we assume local thermodynamic equilibrium, all dust grains have the same temperature which is equal to the gas temperature. We can define this temperature as the temperature of the cell, given by the radiative equilibrium equation :

$$4\pi \int_0^\infty \kappa_i^{\text{abs}}(\lambda) B_\lambda(T_i) d\lambda = 4\pi \int_0^\infty \kappa_i^{\text{abs}}(\lambda) J_\lambda d\lambda \quad (2.20)$$

which we write :

$$\int_0^\infty \kappa_i^{\text{abs}}(\lambda) B_\lambda(T_i) d\lambda = \frac{L_*}{4\pi V_i N_\gamma} \sum_{\lambda, \gamma} \kappa_i^{\text{abs}}(\lambda) \Delta l_\gamma . \quad (2.21)$$

If there is no thermal coupling (other than radiative) between gas and dust, and then between the different dust grain sizes, each grain size has its own temperature and the radiative must be, in this case, written independently for each size :

$$4\pi \int_0^\infty \kappa_i^{\text{abs}}(\lambda, a) B_\lambda(T_i(a)) d\lambda = 4\pi \int_0^\infty \kappa_i^{\text{abs}}(\lambda, a) J_\lambda d\lambda \quad (2.22)$$

where  $\kappa_i^{\text{abs}}(\lambda, a)$  and  $T_i(a)$  are the opacity and temperature of the dust grains of size  $a$  in the cell  $i$ .

The calculation of  $\int_0^\infty \kappa_i^{\text{abs}}(\lambda) B_\lambda(T_i) d\lambda = \sigma T^4 \kappa_P / \pi$  ( $\kappa_P$  is the Planck mean opacity) is very time consuming and we pretabulate these values at  $N_T = 1000$  logarithmically spaced temperatures ranging from 1K to 1500K. The temperature  $T_i$  of each cell is obtained by interpolation between the tabulated temperatures.

Following Bjorkman & Wood (2001), we use the concept of *immediate reemission*. When a packet is absorbed, it is immediately reemitted and its wavelength is chosen taking into account the temperature correction following the probability distribution :

$$p_\lambda d\lambda \propto \kappa_i^{\text{abs}}(\lambda) \left( \frac{dB_\lambda}{dT} \right)_{T_i} d\lambda . \quad (2.23)$$

### 3 Benchmark problem

In order to test MCFOST, we calculated the same cases as described in P04 and compared the results. The geometry tested involves a central point-like source radiating as a  $T=5800\text{K}$  blackbody encircled by a disk of well defined geometry and dust content. The disk extends from 1 AU to 1000 AU. It includes spherical dust grains made of astronomical silicate. Grains have a radius of  $0.12 \mu\text{m}$  and a density of  $3.6 \text{ g.cm}^{-3}$ . The optical data are taken from Draine & Lee (1984). The disk is flared with a Gaussian vertical profile  $\rho(r, z) = \rho_0(r) \exp(-z^2/2h(r)^2)$ . Power-law distributions are used for the surface density  $\Sigma(r) = \Sigma_0 (r/r_0)^\alpha$  and the scale height  $h(r) = h_0 (r/r_0)^\beta$  where  $r$  is the radial coordinate in the equatorial plane,  $h_0$  the scale height at the radius  $r_0$ . These assumptions lead to a general expression for the density at any point in the disk :

$$\rho(r, z) = \rho_0 \left( \frac{r}{r_0} \right)^{\alpha-\beta} \exp \left( -\frac{1}{2} \left( \frac{z}{h(r)} \right)^2 \right) . \quad (3.1)$$



In this benchmark,  $\beta = 1.125$ ,  $\alpha - \beta = -1.0$  are used. The reference radius is  $r_0 = 500$  AU, the disk height is  $h_0 = 99.74$  AU. This scale height is the same as described in P04. A factor  $\sqrt{2/\pi}$  appears because of the different definition of the Gaussian profile in MCFOST<sup>1</sup>.

The scattering is set to be isotropic and polarisation is not calculated, *i.e.*, all the scattering information is contained in the scattering cross section alone,  $Q_{sca}$ , acting on the I Stokes parameter only.

Results are shown in the section below for 4 different disk equatorial optical thicknesses,  $\tau_V$  : 0.1, 1, 10, and 100. For each optical thickness case, results for three different disk inclinations are calculated,  $12.5^\circ$ ,  $42.5^\circ$  and  $77.5^\circ$ .

## 4 Results

### 4.1 Computational considerations

For the test cases considered here, the number of grid cells is set to  $N_r = 50$  and  $N_z = 20$  in the radial and vertical directions.  $10^7$  photon packets are used to calculate the temperature distribution (step 1) and  $2 \cdot 10^6$  photon packets per wavelength are used for the generation of the SED (step 2). The total runtime is 13 minutes for the most optically thin case and 20 minutes for the most optically thick case on a bi-processor (Intel Xeon) computer running at a clockrate of 2.4 GHz. The runtime memory space needed is 10 MBytes.

For the high resolution models (see sec. 4.5 below), with  $N_r = 500$  and  $N_z = 200$ , the runtime for the most optically thick case is  $\approx 7$  hours and the memory occupation is 450 MBytes.

### 4.2 The temperature profiles

The radial and vertical temperature profiles for the most optically thick case are shown in the top panels of Fig. 1 and 2. For clarity the results of MCFOST are shifted by 200 K in Fig. 1 and by 40 K in Fig. 2. The lower panels of both figures show the difference, given in percents, taking the code RADICAL as a reference. The thick solid lines traces the difference of MCFOST with RADICAL. The radial temperature of MCFOST does not differ by more than 5% from all the other codes, except from MC3D and RADICAL close to the inner radius of the disk, and from STEINRAY at large radius, but the maximum difference remains below 15%. In the vertical direction, MCFOST always agrees better than 2.5% with RADICAL, MCTRANSF and RADMC. The agreement with MC3D and STEINRAY is always better than 2.5% at high altitudes ( $\theta > 20^\circ$ ). Closer to the midplane deviations are larger but do not exceed 4%.

---

<sup>1</sup>See the definition of  $f_2(r)$  in eq. 4 of P04.

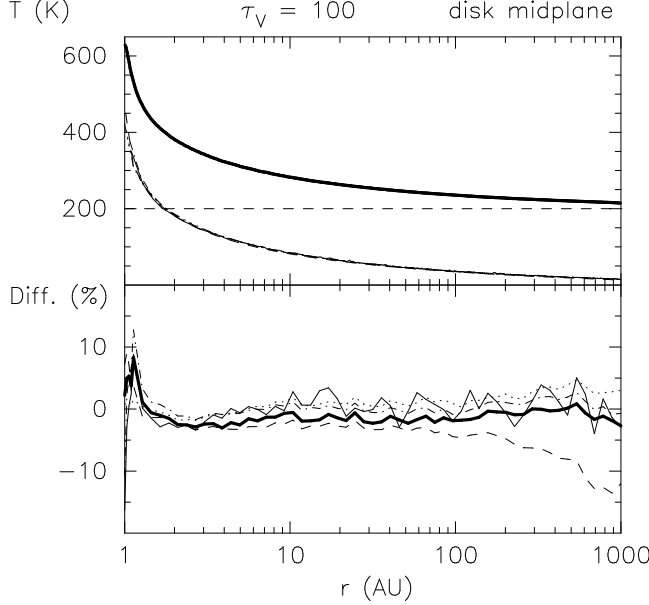


**Fig. 1.** Plots of the radial temperature (upper panel) and the difference (lower panel) for the most optically thick case,  $\tau_V = 100$  and using RADICAL as the reference. In both panels, the results of MCFOST are represented by the thick solid line. Thin solid lines are the results from MC3D, dot-dashed lines from MCTRANSF, dashed-dot-dot-dot from RADICAL, dotted lines from RADMC and dashed lines from STEINRAY. In the upper panel, and all curves being very similar, MCFOST has been shifted by 200K for clarity.

### 4.3 The spectral energy distributions

Shown in Fig. 3 are the calculated SEDs for two disk inclinations and four different optical thickness,  $\tau_V$ . The figure directly compares with Fig. 7 of P04. We plot  $\lambda F_\lambda$  in ( $\text{W.m}^{-2}$ ) where  $F_\lambda$  is the flux density at a distance equal to the stellar radius, for a naked star (without disk)  $F_\lambda = \pi B_\lambda$  (triangles in Fig. 3). MCFOST reproduces the correct slope at long wavelengths, *i.e.*,  $\lambda F_\lambda \propto \lambda^{-5}$ , expected for an optically thin medium containing small particles (with  $\kappa \propto \lambda^{-2}$ ), emitting at long wavelength ( $B_\lambda \propto \lambda^{-4}$ ).

In Fig. 5, the difference of the SEDs calculated by the various RT codes are presented. The overall agreement is better at lower inclinations, a consequence of the lower optical depth along the observer's line of sight. Indeed, for models with  $\tau_V = 0.1$  and  $\tau_V = 1$  at all inclinations and for models with  $\tau_V = 10$  and  $\tau_V = 100$  at inclinations of  $12.5^\circ$  and  $42.5^\circ$ , deviations between MCFOST and all the other codes do not exceed 10%. For the most optically thick cases, *i.e.*, large inclination and/or large optical thickness, the largest differences are observed below  $1\mu\text{m}$ , where scattering dominates, and around  $10\mu\text{m}$ , in the silicate band.

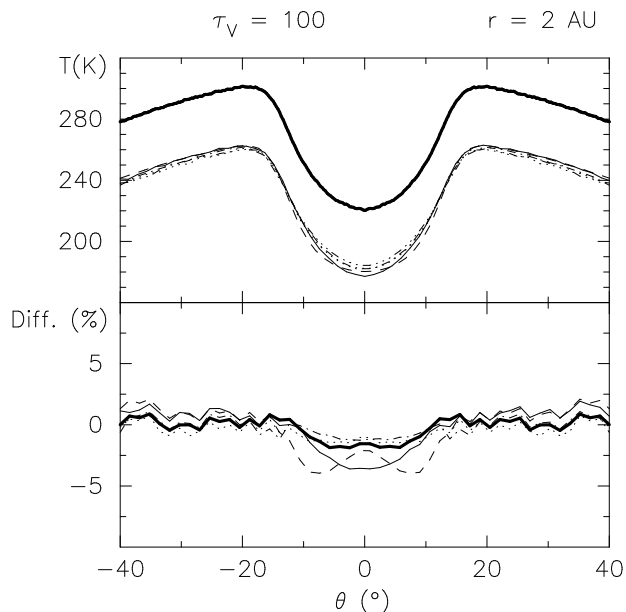


**Fig. 2.** Plots of the vertical temperature (upper panel) and the difference (lower panel) among the codes using RADICAL as the reference, for the most optically thick case,  $\tau_V = 100$  and for a distance  $r$  in the midplane equal to 2 AU from the central star. In the upper panel, the results of MCFOST are shifted by 40 K for clarity. The line types are the same as in Fig. 1.

In the optical range, MCFOST produces slightly larger fluxes with respect to other codes but the large dispersion observed in all codes does reflect lower signal to noise ratio due to lower emerging fluxes. Near  $10\mu\text{m}$ , MCFOST shows the same trend as MCTRANSF but finds larger fluxes than RADICAL or MC3D.

To accelerate convergence in MCFOST, photon packets are recorded in inclination bins that cover a range of angles, instead of a single angle as is often done elsewhere. It is important to note that by doing so, the uncertainty associated with the models easily matches the observational errors. Observationally, inclination angles of disks are rarely known to better than 5-10 (1-2) degrees when seen pole-on (edge-on). In MCFOST, the inclination bins intercept equal solid angles from pole-on to edge-on, *i.e.*, they cover equal intervals in  $\cos i$ . This interval can be set to match the quality of the data. In the calculations presented in this paper, 21 bins are used from pole-on to edge-on. In all figures, the inclinations listed, *i.e.*,  $12.5^\circ$ ,  $42.5^\circ$ ,  $77.5^\circ$ , are the median of the bins covering an interval of 0.05 in  $\cos i$ . These bins have inclinations ranging from  $0^\circ$  to  $17.75^\circ$ , from  $40.37^\circ$  to  $44.42^\circ$ , and from  $76.22^\circ$  to  $79.02^\circ$ , respectively.

For comparison, the axis ratio of a circular disk estimated with a measurement error equal to half the bin width used in this paper, *i.e.*, 0.025, would yield an

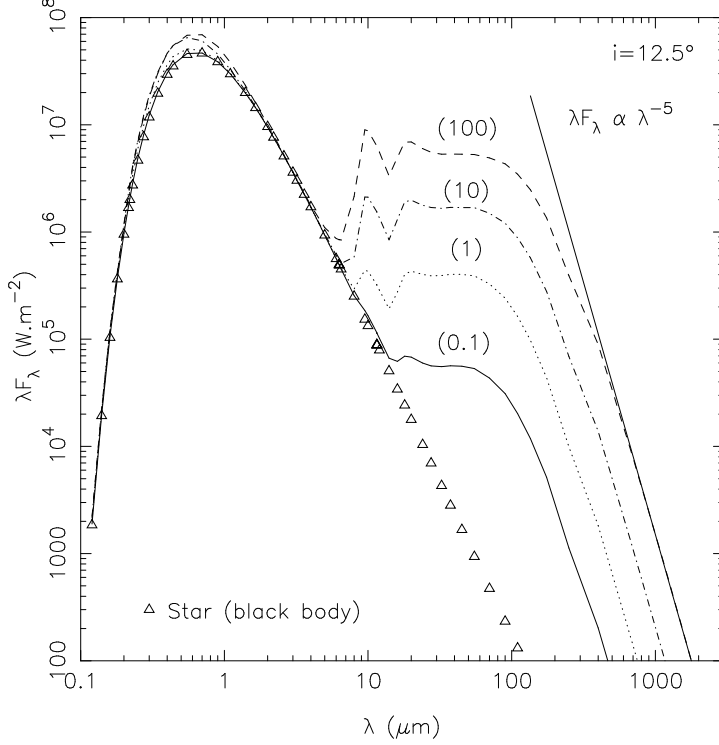


**Fig. 3.** SED for a disk inclination  $i = 12.5^\circ$ . Each curve traces a model SED calculated by MCFOST. The midplane optical depth is given in parenthesis above each curve. The solid lines show results for the most optically thin disk,  $\tau_\nu = 0.1$ , dotted lines for a disk having  $\tau_\nu = 1$ , dot-dashed lines for a disk with  $\tau_\nu = 10$ , and dashed lines for the most optically thick model,  $\tau_\nu = 100$ . The diamonds trace the black-body emission from the naked star. The slope of the SED at long wavelengths depends only on the dust properties and is plotted in each panel with a solid line,  $F_\lambda \propto \lambda^{-6}$ .

error on  $i$  of  $\sim 10^\circ$  for the pole-on case, and  $\sim 1.5^\circ$  in the edge-on case. Indeed, for a perfectly circular pole-on disk, measuring an axis ratio of 0.975 instead of 1.0 would mimic an inclination of  $i = 12^\circ$  instead of  $i = 0^\circ$ . In the edge-on case, measuring an axis ratio of 0.1 instead of 0.125 would induce a difference of  $1.4^\circ$  in the determination of the inclination. The results presented here, generally obtained using 21 inclination bins, are therefore accurate enough and not limited by our choice of inclination bin number.

#### 4.4 Impact of inclination angle sampling

To verify further that an inclination range (as used) does not introduce a noticeable bias in our comparisons, we show in Fig. 9 the same calculations for inclination

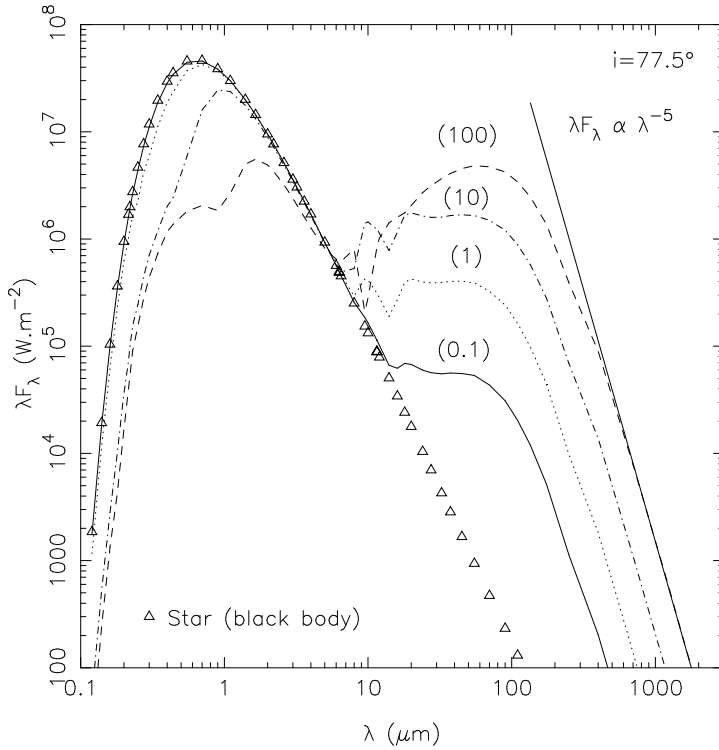


**Fig. 4.** Same as Fig. 3 for an inclination angle of  $i = 77.5^\circ$

bins 20 times narrower. In Fig. 9, the bins run from  $11.76^\circ$  to  $12.89^\circ$ ,  $42.31^\circ$  to  $42.67^\circ$  and from  $77.38^\circ$  to  $77.63^\circ$ . The results are similar to those of Fig. 5, bottom right panel.

#### 4.5 Impact of grid sampling

In this section, we test the influence of the grid sampling on the resulting SEDs. In Fig. 10, the difference between the previous calculations with  $\tau_V = 100$  and the same calculations performed with a grid sampling 10 times finer, both in radial and vertical direction are shown. The number of the photons is the same for the two simulations. The high resolution calculations were done with the same number of photons as previously, the corresponding runtime is  $\approx 7$  hours. The comparison shows that the spatial resolution has very little influence on the SED, with differences not exceeding 2.5% even in the worst case.

#### 4.6 Impact of vertical cutoff

MCFOST is the only code which uses a cylindrical grid and introduces a vertical cutoff for the density, all other code have adopted spherical geometries and

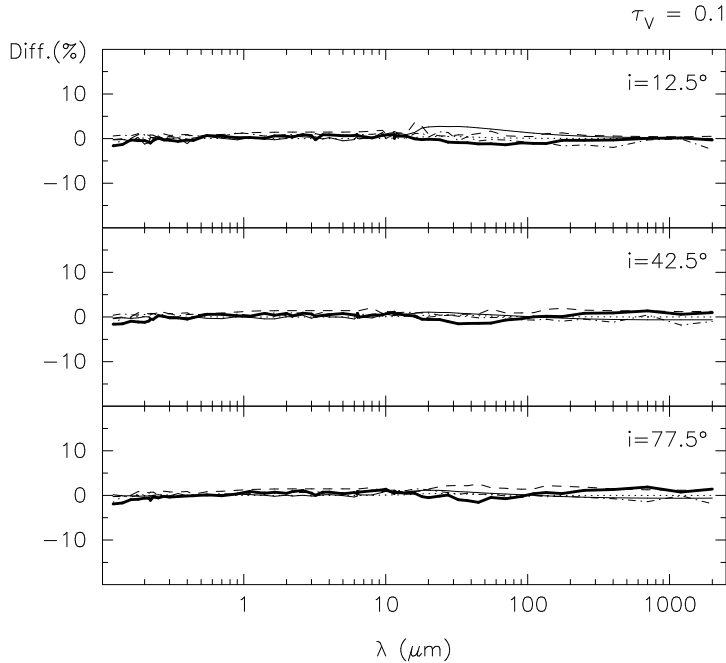


**Fig. 5.** Plots of the difference between the model SED, given in percents, using the code RADICAL as the reference. Results from all codes are shown: the five codes included in the study of P04 and MCFOST (this study). Results are shown as a function of optical thickness of the disk midplane and as a function of inclination angle. Results are shown for the most optically thin case  $\tau_V = 0.1$ . Three different inclination angles are considered:  $i = 12.5^\circ$  (upper),  $i = 42.5^\circ$  (middle), and  $i = 77.5^\circ$  (lower). All codes are compared to RADICAL. The thick solid line gives the differences for MCFOST, the thin solid line for MC3D, the dot-dashed line for MCTRANSF, the dotted line for RADMC, and the dashed lines for STEINRAY.

do not need to set up a vertical cutoff. The cutoff is generally chosen at 10 times the local scale height of the disk. The corresponding density is equal to  $\exp(-10^2/2) \approx 2 \cdot 10^{-22}$  times the density in the midplane of the disk and is so low that no absorption or scattering actually occurs in this region. To verify the influence of the cutoff on the emerging spectra, we run the previous models with a cutoff of 20 times the scale height rather than 10, keeping the same vertical resolution and then using twice more cells. The difference between the models with a cutoff at 10 and 20 times the scale height are shown in Fig. 11. They always stay below 3 % even at the highest optical depth.

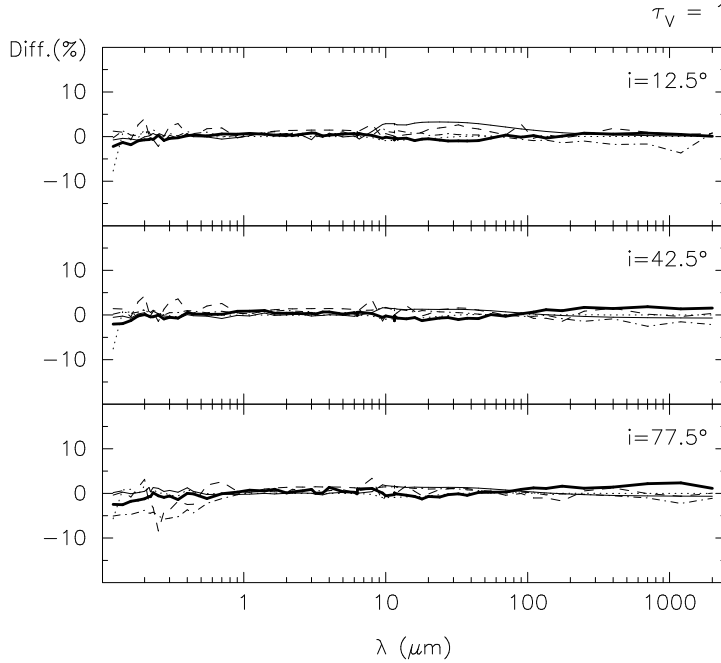


**Fig. 6.** Same as figure 5 but for  $\tau_V = 1$ .

## 5 Discussion and conclusions

In the sections above we presented a new continuum 3D radiative transfer code, MCFOST. The efficiency and reliability of MCFOST was tested by considering a simple and well-defined problem, a dusty disk as described in P04, that was used as a benchmark to compare MCFOST with 5 other RT codes. MCFOST was shown to calculate temperature distributions and SEDs that are in excellent agreement with previous results from the other codes. The results of MCFOST for all the test cases are available at the web site : <http://www-laog.obs.ujf-grenoble.fr/~cpinte/mcfost/>.

Because MCFOST reproduces well the results presented in P04, their conclusions also hold for MCFOST. In particular, we find that the far-infrared part of the SEDs is unaffected by the viewing angle, see Fig. 3. On the other hand, the spectrum at shorter wavelengths is largely modified, with the stellar spectrum dominating for pole-on views and becoming progressively more attenuated with increasing viewing angle. For cases with large attenuation of the starlight (high inclinations and large optical depths) the contribution from scattering becomes important because the dust grains have a high albedo. Also, the spectroscopic signatures of silicates at  $10\mu\text{m}$  and  $20\mu\text{m}$  are visible, as expected. The overall temperature profiles in the disk and shape of the emerging SEDs are well reproduced by MCFOST. Differences in the radial temperatures computed by MCFOST do not exceed 4% with respect to the other 5 codes in the optically thin case. For

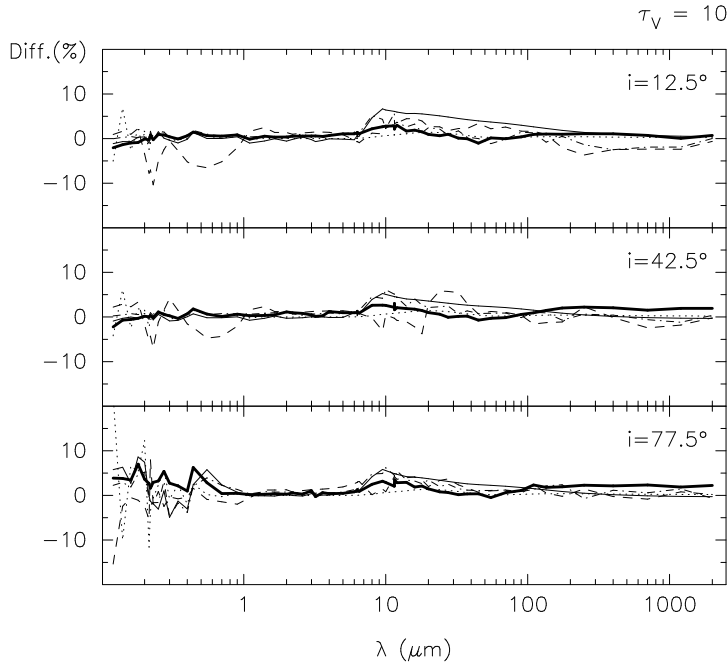


**Fig. 7.** Same as figure 5 but for  $\tau_V = 10$ .

the most optically thick case, differences do not exceed 15%. Regarding SEDs, MCFOST is similar to all other codes to better than 10% for low optical thickness. Deviations as large as 15% are however observed in the most defavorable case, *i.e.*, high tilt and optical thickness, except with STEINRAY which deviates from all other codes, between 10 and 30  $\mu\text{m}$  (see P04 for more detailed description of these deviations).

In this paper, disks with fairly low equatorial V-band optical depths were calculated,  $\tau_V = 100$ . To reproduce observed edge-on disks, MCFOST has been able so far to handle more compact, equatorially concentrated disks with  $\tau_V \sim 10^6$ , illustrating the ability of MCFOST to model much more optically thick disk than the one used for the benchmark simulation

Various tests were further performed to show the independence of the MCFOST results with respect to grid sampling, inclination sampling, and position of the vertical density cut-off in the disk. Results are not noticeably affected.

## References

- Bjorkman, J. E. & Wood, K. 2001, ApJ, 554, 615  
 Cashwell, E. & Everett, C. 1959, A practical manual on the Monte Carlo Method for random walk problem (Pergamon, New York)



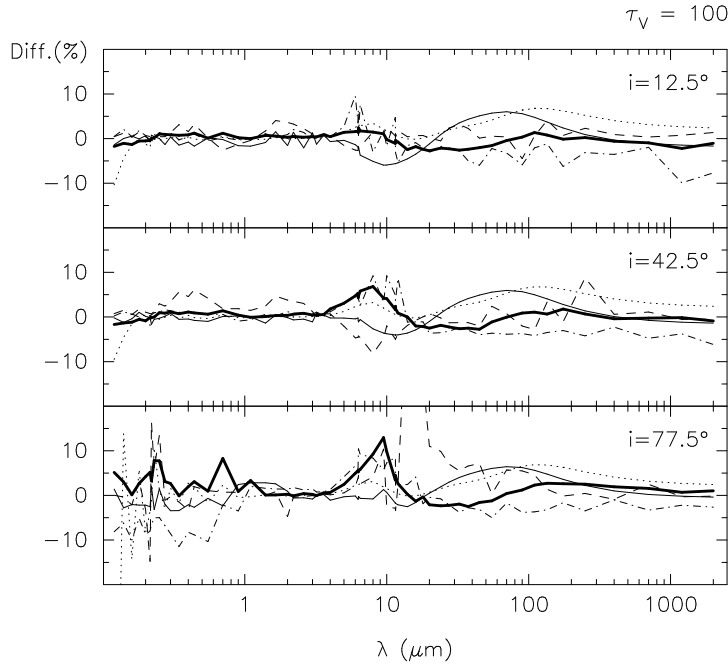


**Fig. 8.** Same as figure 5 but for  $\tau_V = 100$ .

- Chrysostomou, A., Ménard, F., Gledhill, T. M., Clark, S., Hough, J. H., McCall, A., Tamura, M. 1997, MNRAS, 285, 750
- Draine, B. T. & Lee, H. M. 1984, ApJ, 285, 89
- Duchêne, G., McCabe, C., Ghez, A. M., & Macintosh, B. A. 2004, ApJ, 606, 969
- Lucy, L. B. 1999, A&A, 345, 211
- Ménard, F. 1989, PhD thesis, Université de Montréal
- Monin, J.-L., Ménard, F., & Duchêne, G. 1998, A&A, 339, 113
- Pascucci, I., Wolf, S., Steinacker, J., Dullemond, C.P., Henning, T., Niccolini, G., Woitke, P., & Lopez, B. 2004, A&A, 417, 793
- Pinte, C. & Ménard, F. 2004, in AIP Conf. Proc. 713: The Search for Other Worlds, 123–126
- Solc, M. 1989, Astronomische Nachrichten, 310, 329

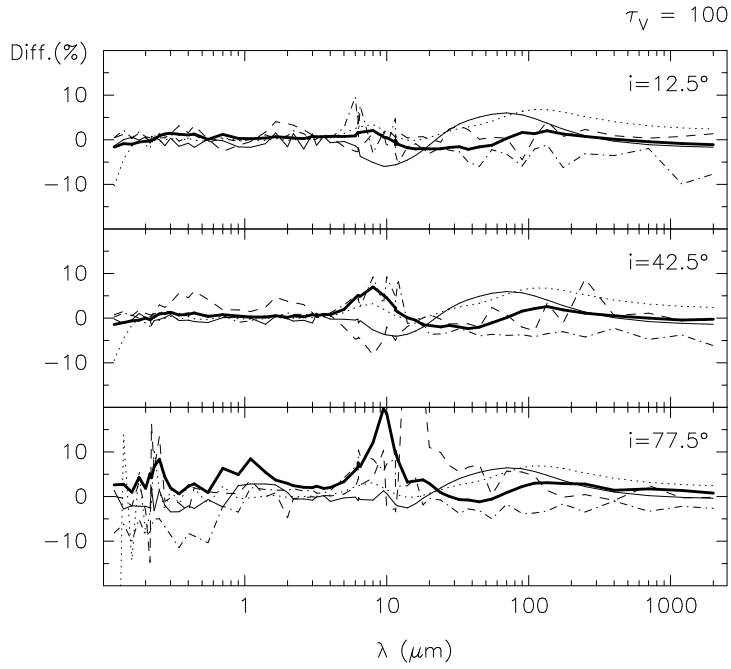


**Fig. 9.** Plots of the difference of the results MCFOST and other codes for the most optically thick case with high resolution on inclination bins. The figure presents the same calculations as the bottom-right panel of Fig. 5 but with 20 times narrower inclination bins. The lines type are the same as in Fig. 5.

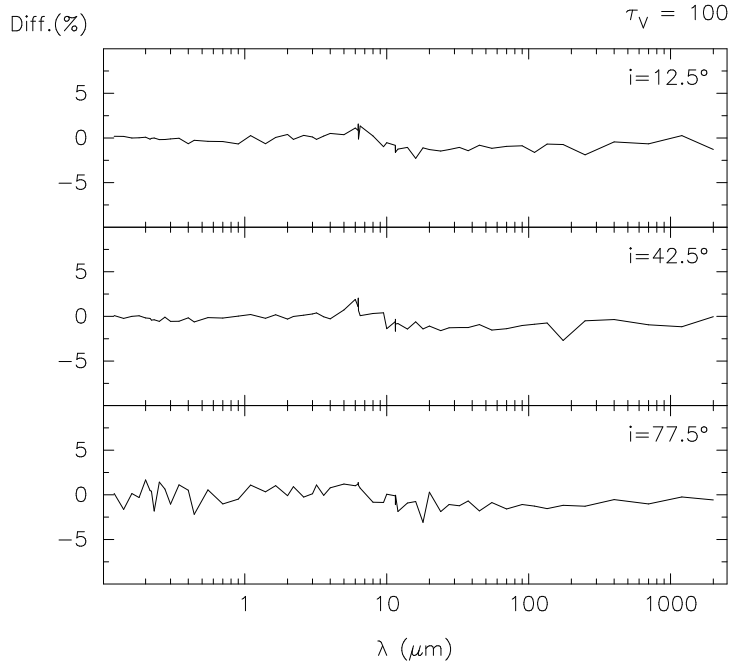


**Fig. 10.** Spatial resolution tests. Difference percentage between the emerging SED of the model with a grid of  $(500 \times 200)$  points (radial  $\times$  vertical) and the reference model with a grid of  $(50 \times 20)$  points. The number of “photons packets” is the same for the two models.

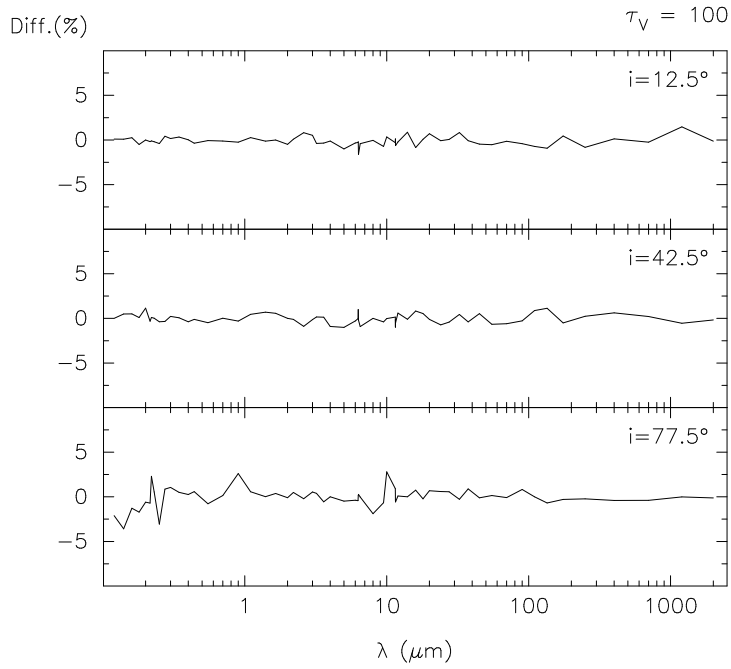


**Fig. 11.** Effect of the vertical cutoff. We plot the difference, given in percents, of the model with a vertical cutoff at 20 times the scale height relative to the reference model plotted in 3 (cutoff at 10 times the scale height) for the most optical thick case. The two models have the same vertical resolution.